

The strain-induced martensitic phase transformation of Fe–C alloys considering C addition: A molecular dynamics study

Ye Jiao, WenJiao Dan^{a)}, WeiGang Zhang

Department of Engineering Mechanics, School of Naval Architecture, Ocean and Civil Engineering, Shanghai Jiao Tong University, Shanghai 200240, China

^{a)}Address all correspondence to this author. e-mail: wjdan@sjtu.edu.cn

Received: 18 December 2019; accepted: 1 June 2020

This study investigates the effect of C on the deformation mechanisms in Fe–C alloys by molecular dynamics simulations. In uniaxial tensile simulations, the face-centered-cubic (fcc) structures of Fe–C alloys undergo the following deformation processes: (i) fcc→body-centered-cubic (bcc) martensitic transformation, (ii) deformation of bcc phase, and (iii) bcc→hcp martensitic transformation, which are significantly influenced by the C concentration. For the low C concentrations (0–0.8 wt%) fcc phase, the fcc→bcc phase transformation accords a two-stage shear transformation mechanism based on the Bain model, the deformation mechanism of the bcc phase is the first migration of twinning structures and then elastic deformation, and the bcc→hcp phase transformation follows Burgers relations resulting from the shear of the bcc close-packed layers. However, for the fcc phase with high C concentrations (1.0–2.0 wt%), the fcc→bcc phase transformation follows a localized Bain transformation mechanism impeded by the C atoms, the bcc phase only experiences elastic deformation, and the bcc→hcp phase transformation also conforms to Burgers relations but become localized due to the addition of more C atoms. Because of the different phase transformation mechanisms between the high C and low C supercells, the dislocation generation mechanism is also different.

INTRODUCTION

The martensitic transformation is an important solid-state phase transformation in pure metals and alloys. It is a diffusionless-type phase transformation achieved by the cooperative movement of atoms at distances less than the diameter of the atoms and accompanied by changes in the crystal structure and macroscopic shape [1]. Generally, the phase transformation is caused by the free-energy difference between the two phases, which is influenced by the pressure and the temperature, but it has been found that the martensitic transformation can also be generated by external strains [2], namely the strain-induced martensitic transformation. In 1924, Sauveur [3] discovered that this kind of martensite formation resulted in a significant increase in the ductility of the steel. This phenomenon is known as transformation-induced plasticity (TRIP). Steels with such property are widely used in the automobile industry.

The practical application of martensitic transformation has attracted a great deal of effort to explore the theory of martensite

crystallography [4,5]. In 1924, Bain [6] postulated a tetragonal deformation mechanism that would be capable of converting the face-centered-cubic (fcc) austenite to body-centered-cubic (bcc) or body-centered-tetragonal (bct) martensite in carbon steel. Based on the Bain model, Kurdjumov and Sachs [7] suggested a shear mechanism along the $[112]_{fcc}$ direction in the $(111)_{fcc}$ plane. Nishiyama [8] derived a similar model but with a principal shear along the $[101]_{fcc}$ direction in the $(111)_{fcc}$ plane. Burgers [9] proposed a crystallography mechanism of bcc↔hcp transformation in Zr achieved by atomic shear along the $[111]_{bcc}$ direction in the $(110)_{bcc}$ plane. A theory of strain-induced martensitic nucleation was developed by Bogers and Burgers (B–B) [10]. They described this process was achieved by two intersection shear along the close-packed planes which is in the same direction as the normal twinning shear. Olson and Cohen [11] extended the B–B model by introducing the dislocation theory of martensitic transformations. The recently developed phenomenological theory of martensite

crystallography (PTMC) is a phenomenological nature theory and presumes that the lattice between two phases is corresponding and the planar interface of martensite must be an invariant plane during the phase transformation [12]. However, all these theoretical models are based on the crystal structure change between the parent crystal and the transformation product, and the details of atomic motion during the transformation process are still unclear. Due to the quite rapid velocity of martensite formation (in excess of 1000 m/s^{-1}) [13], it is difficult to experimentally observe the atomic motion during this process.

In recent years, advances in molecular dynamics (MD) and interatomic potentials make it possible to investigate the phase transformation mechanism reliably. MD methods can achieve up to 1-ms simulation process with a time scale of nanoseconds (10^{-9} s). Additionally, the MD visualization and analysis softwares like OVITO [14] and AtomEye [15] have demonstrated their superiority in observation of the atomic movement in three dimensions. These methods enable us not only to observe the martensitic transformation process step by step, but to measure the stress, potential energy, and other properties of atoms [16,17]. The earliest MD simulation study of martensitic transformation in pure Fe was performed by Entel et al. [18]. They generated a reliable potential that can reproduce the bcc \leftrightarrow fcc structural changes, which is by far the most widely used for studying austenitic and martensitic transformations in the pure Fe system. In a more recent study, Karewar et al. [19] investigated the effect of defects on martensitic transformation in pure Fe during the cooling process and concluded that the atomistic martensitic transformation mechanism depended on the type of the defects. However, until now, there have been few studies on the martensitic transformation of ferroalloy. It is well known that C is one of the most important basic alloying elements in steel and can affect markedly the deformation mechanisms of steels by distorting the lattice and generating the short-range strains [20]. The C atoms trapped in the defect lattice also control the kinetics of the martensitic transformation process [21]. To study the role of C in this process, Wang et al. [17] investigated the bulk Fe–C systems and found that the martensitic transformation temperature decreased with C content. Then, they studied the temperature- and strain-induced martensitic transformation in Fe–C nanowires [22]. Karewar et al. [23] explored the temperature-induced martensitic transformation in the Fe–C system with pre-defects and proved that the C atoms increased the critical atomic shear stress which significantly influenced the martensitic transformation. Luu and Gunkelmann [24] studied the role of C on the bcc \rightarrow hcp martensitic transformation under pressure and found that C atoms increased the transformation pressure. So far, the investigation of strain-induced martensitic transformation of Fe–C materials in the atomic process is scarce and the effect of C atoms on the transformation mechanism still remains elusive.

In this study, the strain-induced martensitic transformation mechanisms of the fcc structure Fe–C alloys under uniaxial tensile was investigated by MD methods. The effect of the C atoms on the deformation mechanisms was investigated at the atomic scale and focused on the following aspects of the deformation process: Mechanical response of the deformation process, fcc \rightarrow bcc martensitic transformation mechanism, bcc deformation mechanism, bcc \rightarrow hcp martensitic transformation mechanism, and dislocation analysis during the phase transformations.

RESULTS AND DISCUSSION

The mechanical responses and phase transformation mechanisms of the supercells with the same C concentration are almost the same although the specific C atoms distribution is different. For different sizes of the supercells, the phase transformation mechanism is the same and the mechanical response is slightly different, but it also reflects the phase transformation process. The stress–strain curves of different size supercells of 0.2 wt% C concentration are shown in Supplementary Material S1. Therefore, the simulation results of the supercells of size $10\times 10\times 10$ are displayed for better observation.

Mechanical response and phase transformation of the deformation process

The X-axis stress–strain curves of the tensile deformation for various C concentration supercells are displayed in Figs. 1(a) and 1(b). As can be seen, the stress–strain curves of the supercells with low C and high C concentrations are quite different. For low C concentrations (0, 0.2, 0.4, 0.6, and 0.8 wt%) as shown in Fig. 1(a), the stress curves fluctuate sharply in the strain range of about 3–8%. The stress then drops to the minimum point, and afterward, a linear increase of stress ensues. Once the stress reaches the maximum point, it declines steeply again. In contrast, there is no violent fluctuation in the stress curves of high C concentrations (1.0, 1.2, 1.4, 1.6, 1.8, and 2.0 wt%), as shown in Fig. 1(b). The mechanical responses are usually the result of microstructural changes. In this regard, it is essential to review the local atomic structure change during the deformation process.

The deformation mechanism of low C and high C supercells is quite different. Therefore, a representative supercell of each type is selected for discussion. Figures 1(c) and 1(d) reveal the atomic structure transformation and corresponding mechanical response of supercell with 0.2 wt% C (representing low C) and 1.4 wt% C (representing high C) concentrations by using the adaptive common neighbor analysis (a-CNA) method, respectively. For 0.2 wt% C shown in Fig. 1(c), at the beginning of the deformation, the simulation supercell

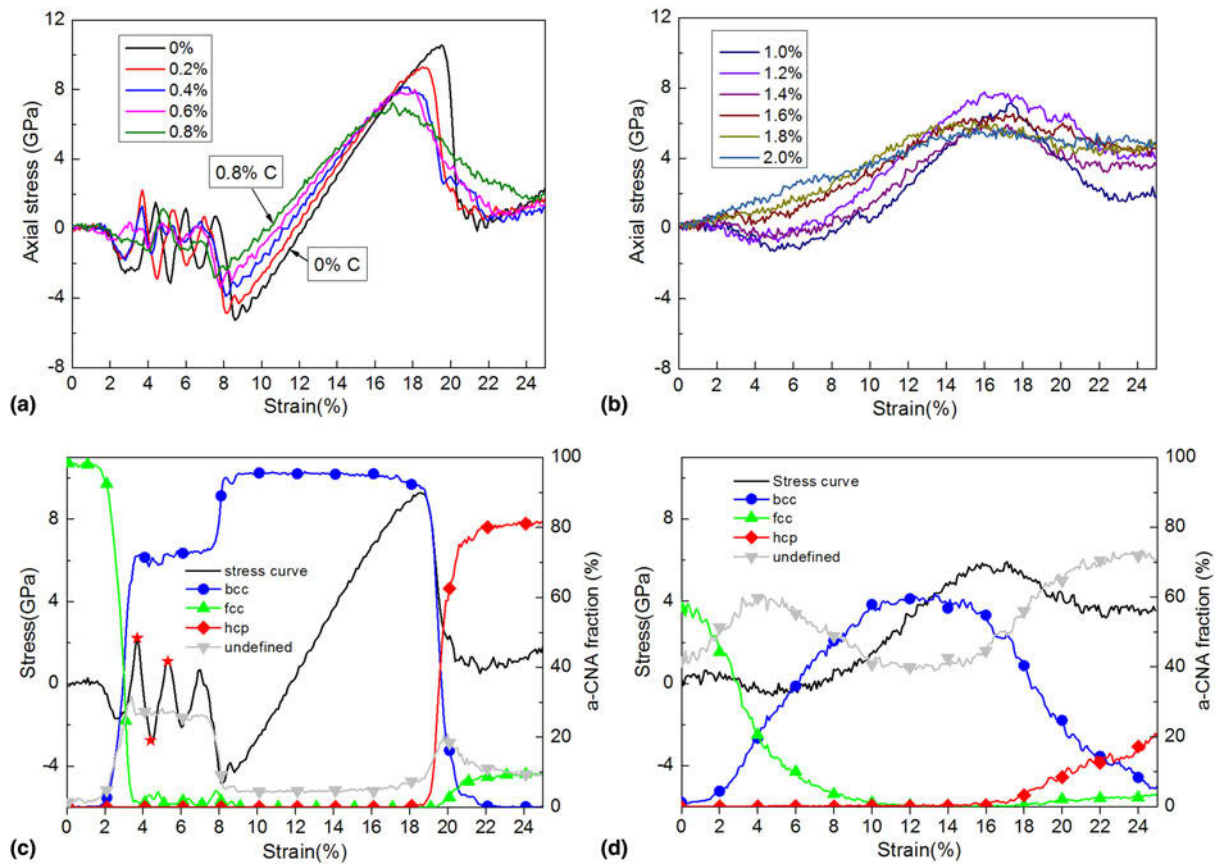


Figure 1: X-axis stress–strain curves for various C concentrations: (a) 0, 0.2, 0.4, 0.6, and 0.8 wt% C concentration. (b) 1.0, 1.2, 1.4, 1.6, 1.8, and 2.0 wt% C concentration. The atomic structure transformation analysis and corresponding stress–strain curve: (c) 0.2 wt% C concentration supercell and (d) 1.4 wt% C concentration supercell.

maintains the initial fcc structure until the strain reaches 2%. At this strain point, the fcc structure starts to rapidly transform into the bcc structure. With further deformation, the fcc→bcc phase transformation completes at $\epsilon = 3.6\%$. During this transition stage, the stress begins to drop rapidly and then sharply increases which may be caused by the two-stage shear deformation. And this mechanism will be discussed in the section “Phase transformation mechanism of fcc→bcc”. Between $\epsilon = 4$ and 8%, the deformation stress rises and decreases repeatedly. At the end of this deformation stage, at about $\epsilon = 7.5\%$, the unidentified atoms transform to bcc structure atoms, which lead to a significant reduction of stress. Next, the new bcc structure exhibits nearly linear elastic deformation behavior, and an interesting distinction is noted that the elastic constant (slope of the stress curve) of the bcc structure decreases as C concentration increases as detailed in Figs. 1(a) and 1(b). The elastic deformation stage of the bcc structure is terminated by the bcc→hcp phase transformation at $\epsilon = 18.5\%$, which causes the stress to drop simultaneously. Both the fcc→bcc and bcc→hcp phase transformations are almost instantaneous in 0.2 wt% C supercell. In contrast, the phase transformations in 1.4 wt% C supercell are significantly slower, as shown in

Fig. 1(d). The corresponding stress curve also declines first and then increases but relatively modest compares with that in 0.2 wt% C supercell. This fcc→bcc phase transformation is a continuous transformation process that starts at the very beginning of the deformation and continues in a wide range of strains from 0 to 12%. Similarly, the bcc→hcp phase transformation of 1.4 wt% C is also a gradual process. To understand the discrepancies of the deformation mechanisms between high C concentration and low C concentration supercells, these deformation mechanisms will be analyzed at the atomic scale in the section “Phase transformation mechanism of fcc→bcc”.

To examine the strain rate effect, the tensile strain rate is set to $1 \times 10^8/s$, $1 \times 10^9/s$, and $1 \times 10^{10}/s$. The stress–strain curves of the 0.2 wt% C supercells at different strain rates are shown in Supplementary Material S2. Seen from the figure, the strain rate has a certain effect on the mechanical response during the deformation process. As the strain rate decreases, the fcc→bcc phase transformation begins to occur at a lower strain and the degree of stress fluctuation of the bcc deformation is reduced. These phenomena may be due to the slower deformation rate allowing the atoms to have more time to relax. Under different

strain rate conditions, the strain point at which the bcc structure begins to elastically deform is almost the same, and the elastic constant (slope of the stress curve) of bcc phase is also the same. On the other hand, the strain at which the bcc→hcp phase transformation occurs decreases slightly as the strain rate decreases. Although the stress–strain curves are unique at different strain rates, all the supercells have undergone the fcc→bcc phase transformation, the deformation of bcc phase, and the bcc→hcp phase transformation, and there is no difference in the nuclear mechanism of phase transformation.

Phase transformation mechanism of fcc→bcc

Figures 2(a)–2(f) show the atomic structure change and atomic displacements in coordinate axis directions of 0.2 wt% C supercell at the strain where the fcc→bcc transformation just completes ($\epsilon = 3.6\%$). The initial fcc structure (green) is shown in Fig. 2(a), and the interstitial C atoms (pink) are in the octahedral sites of fcc structure and cause the lattice distortion and the nearest six Fe atoms unidentified (grey). The bcc structure (blue) after the phase transformation is shown in Fig. 2(b), in which the layers of unidentified atoms (grey) constitute the (101) slip planes, indicating that the atoms would have displaced parallel to these planes. The C atoms in the octahedral site of bcc structure are inherited from the octahedral sites in fcc austenite which causes the lattice distortion and two nearest-neighbor and four second-nearest-neighbor Fe atoms unidentified (grey). In Figs. 2(d)–2(f), the displacement scalar of atoms is colored by the color-coding modifier of OVITO software. The displacements of atoms in the *X*-axis direction are divided by the slip planes, as illustrated in Fig. 2(d), and a similar phenomenon is observed in the *Z*-axis direction, as shown in Fig. 2(f). Figure 2(e) indicates that the atoms deviate from each other in the *Y*-axis direction, which results in a uniform extension of the supercell in this direction. These specific movements of atoms lead to the generation of twinning structures shown in Fig. 2(c), which are characteristic of the real bcc martensite. Similar twinning structures were observed in the previous MD study of Engin and Urbassek [25]. They found that the typical twinning martensite was an intermediate during the temperature-induced martensitic transformation in pure Fe. In our work, the twinning martensite appears in the pure Fe and low C supercells during the deformation simulation. The agreement between our results and theirs suggests that both temperature and external strain could induce the formation of the twinning structures.

In order to further study the fcc→bcc phase transformation mechanism, the sandwiched region between the dotted lines in Fig. 2(e) is chosen to investigate the exact path of atoms, as shown in Fig. 3. Figure 3(a) shows the initial fcc structure. The potential energy of the initial fcc atoms is displayed in

Fig. 3(b). It is evident that the Fe atoms nearest to the C atoms have lower potential energy. This is because C is a strong austenite stabilizer. Because of the low C concentration, most Fe atoms have the same properties and the anisotropy of deformation is small. When the strain reaches 2.9%, the fcc atoms at the four corners and center of the layers change to the bcc structure, as shown in Fig. 3(c). The displacements of atoms are indicated by black arrows, suggesting that the shear deformation which is 45° from the tensile direction has happened in the fcc structure. The exact mechanism of the fcc→bcc transformation is shown in the red rectangular of Fig. 3(d), the atoms move mainly along the *Z*-axis with small components on the *X*- and *Y*-axis, which is in general consistent with the Bain martensitic transformation mechanism. The schematic illustration of the Bain model is shown in Fig. 3(e), in which a bcc unit cell (colored in blue) can be identified in a pair of fcc unit cells (colored in green). The *c*-axis contracts by about 20% and the *a*-axis expands by about 12% during the phase transformation. Figure 3(f) illustrates the angle change of the lattice from fcc to bcc for the atoms in Fig. 3(d), which indicates that the lattice orientation relationships are

$$(001)_{\text{fcc}}(001)_{\text{bcc}} \text{ and } [100]_{\text{fcc}}[110]_{\text{bcc}}$$

As strain reaches 3.2%, almost all fcc atoms that are not in the shear regions have changed into the bcc structure as detailed in Fig. 3(g). Between $\epsilon = 3.2$ and 3.6%, the four shear bands evolve to two complementary shear bands to accommodate more strain and relieve internal stress, according to Fig. 3(h). Meanwhile, the bcc twinning substructures are produced as illustrated by red lines in Fig. 3(h). In this figure, the surface relief can be observed where the bcc twinning plate forms. The bcc twinning substructure and surface relief are the general characteristics of bcc martensite which have been observed in many experiments [26,27,28]. It is not just the atoms of these layers, this shear makes the whole supercell transform into the twinning substructures of bcc martensite, as shown in Fig. 2(b). It is noted that the main effect of the shear deformation of this stage is to force the formation of bcc twinning substructure, which is significantly different from the previous shear that leads to the fcc→bcc transformation. In previous studies, the concept of two-stage shear mechanism has been presented in some theories of martensitic transformation, Kurdjumov and Sachs [7] proposed that an “invisible” shear would happen which led to the formation of internal substructures, such as slip or twinning. Similarly, Greninger and Troiano [29] recognized that the shear of the shape change was unable to drive the fcc→bcc transformation to happen. Hence, they introduced a two-step shear mechanism: one shear was responsible for changing the shape and a second shear caused changes in the crystal structure. Based

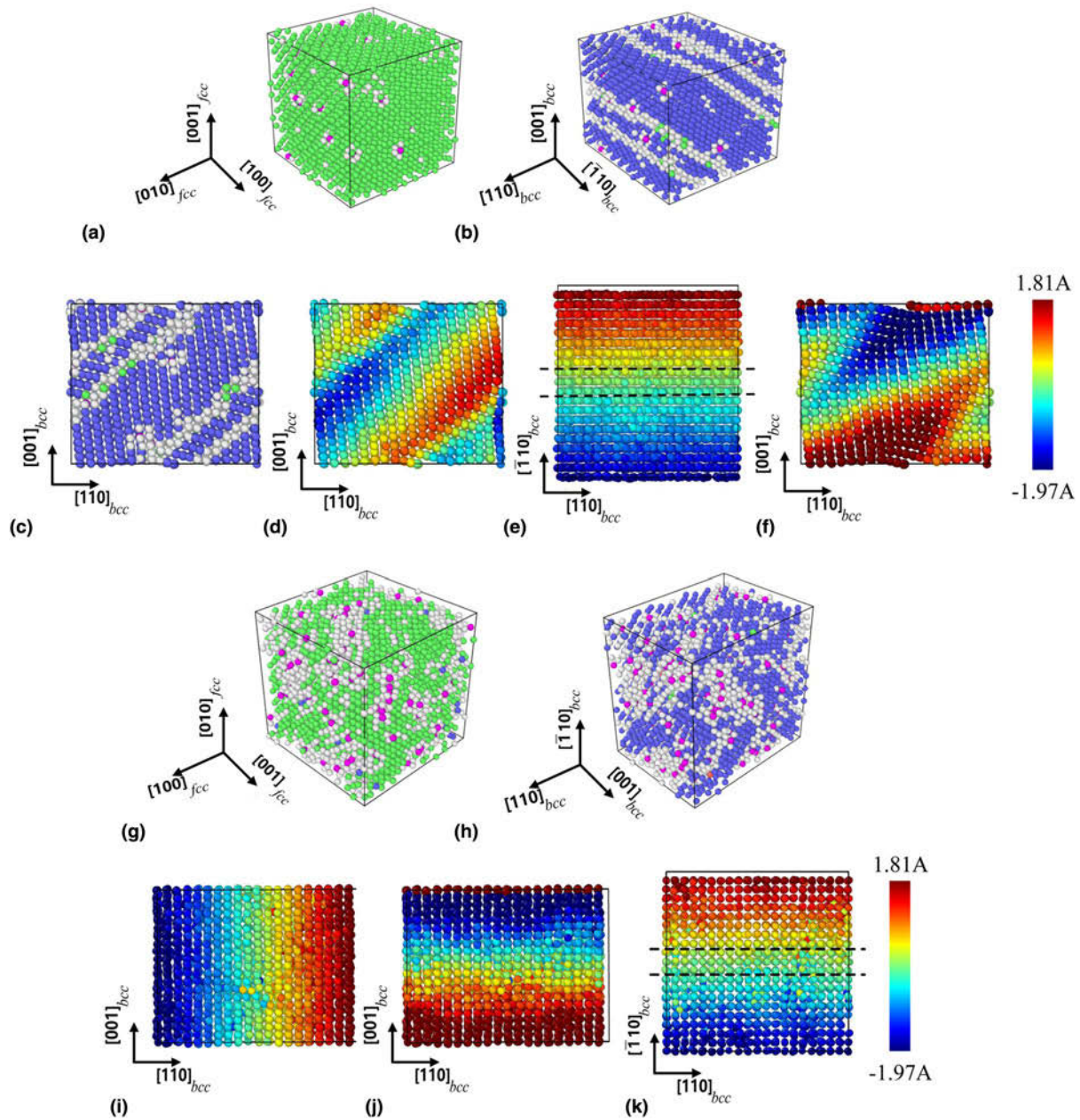


Figure 2: The displacement analysis of fcc→bcc phase transformation for 0.2 wt% C: (a) initial atomic structure of the supercell. After the fcc→bcc phase transformation, the structure is as shown in (b) and (c) at $\epsilon = 3.6\%$. (d–f) Atoms are colored of the displacement scalar at $\epsilon = 3.6\%$ from its original coordinates in the X-axis direction, Y-axis direction, and Z-axis direction, respectively. The displacement analysis of fcc→bcc phase transformation for 1.4 wt% C: (g) initial atomic structure of the supercell. (h) Atomic structure after phase transformation at $\epsilon = 10.5\%$. (i–k) Atoms are colored of displacement scalar at $\epsilon = 10.5\%$ from its original coordinates in X-axis direction, Y-axis direction, and Z-axis direction, respectively. Atoms in (a), (b), (g), and (h) are colored by the a-CNA method: bcc (blue), fcc (green), unidentified (grey), and carbon (pink). Moreover, each layer of the atoms perpendicular to the paper direction has almost the same displacement.

on the Greninger–Troiano double-shear mechanism, PTMC theory [1] introduced a two-step shear mechanism in a matrix algebra manner. Nishiyama [20] also considered that the lattice imperfections (slip or twinning) observed in experiments were the evidence of the second shear mechanism and assumed that the first shear changed the shape of the unit cell and a second shear to relax the transformation simultaneously. In our present simulations, the fcc→bcc transformation process of

0.2 wt% C confirms the two-stage shear mechanism: the first stage shear mainly causes fcc phase to transform into bcc phase, the second stage shear mainly response to the formation of the twinning substructures. Besides, the corresponding mechanical response also indirectly supports this shear mechanism as indicated in Fig. 1(c) between $\epsilon = 2$ and 3.6%, the X-axis stress drops in the first stage shear deformation which is caused by the phase transformation. As the phase

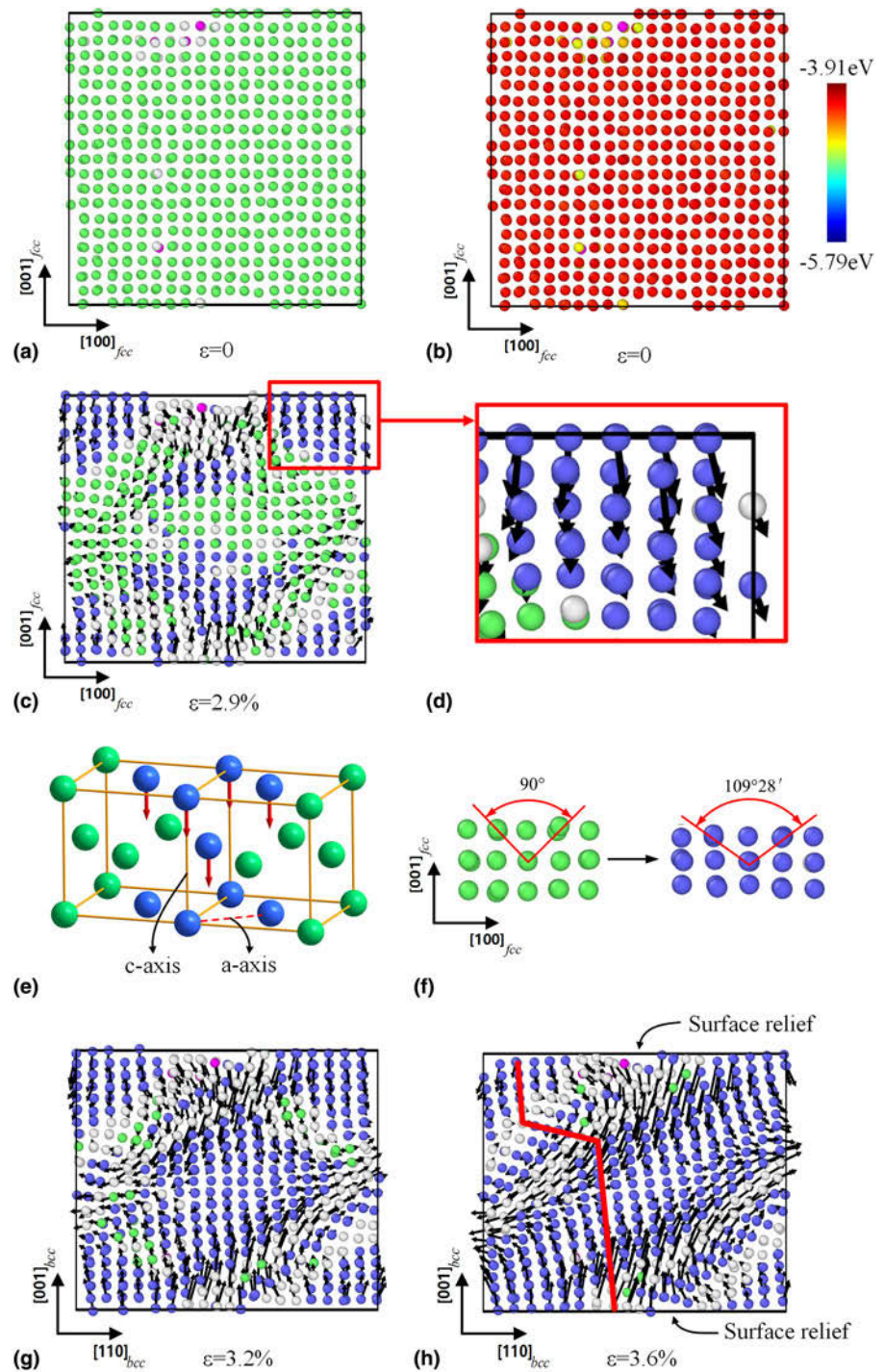


Figure 3: In the path of atoms during the fcc→bcc martensitic transformation, the black arrows represent displacement, which are magnified 1.5 times for better observation. (a) The initial fcc structure. (b) The per-atom potential energy for each atom of the initial fcc structure. (c) $\epsilon = 2.9\%$. (d) Atomic displacements in (c). (e) Schematic illustration of the Bain model. (f) Lattice orientation relationships of atoms in (d). (g) $\epsilon = 3.2\%$. (h) $\epsilon = 3.6\%$. Atoms in (a) and (c–h) are colored by the a-CNA method: bcc (blue), fcc (green), unidentified (grey), and carbon (pink).

transformation continues, the bcc atoms become the majority in the supercell. The deformation mechanism turns into the shear slip of bcc atoms, that is, the second stage shear. Meanwhile, the resistance to slip increases, which causes the X-axis stress to rise.

Figures 2(g)–2(k) provide the atomic structure change and atomic displacements of 1.4 wt% C supercell during the fcc→bcc phase transformation. The initial fcc structure and

the bcc structure martensite after the phase transformation are shown in Figs. 2(g) and 2(h), respectively. The number of Fe atoms affected by the interstitial C atoms is increased compared with the 0.2 wt% C supercell. In addition, the bcc martensite product has no substructure. According to Figs. 2(i)–2(k), the displacement analysis indicates that the atoms stretch evenly in the X- and Z-axis, while contract in the Y-axis which means no two-stage shear mechanism occurs during

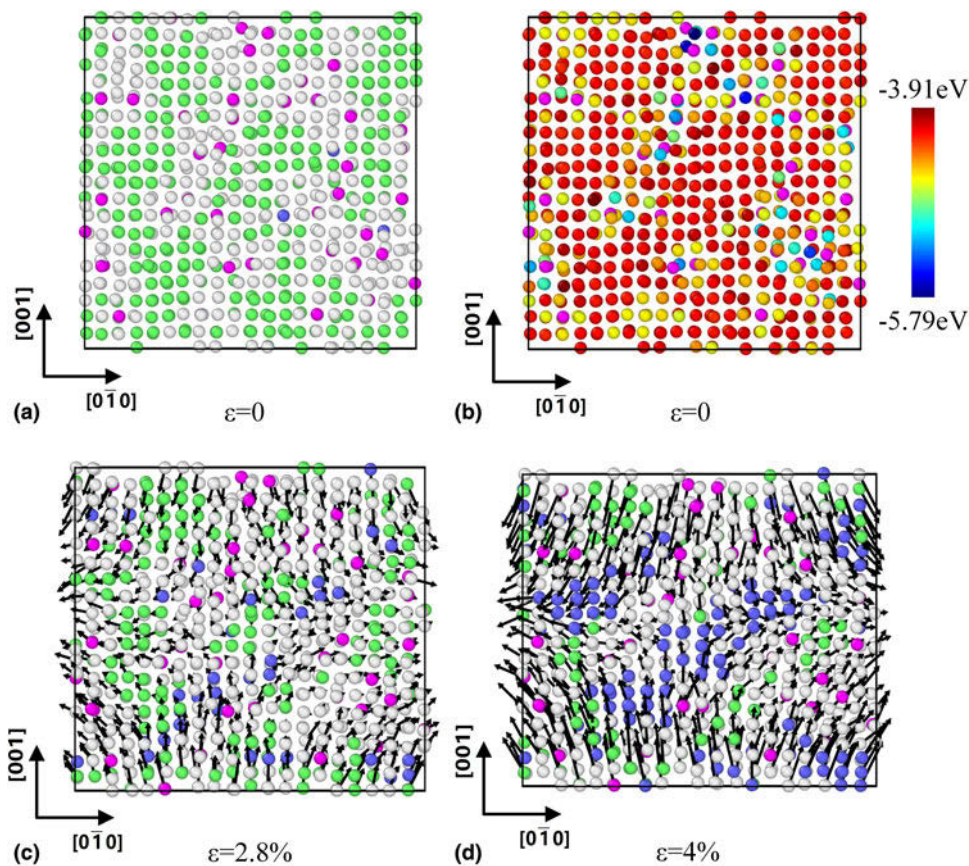


Figure 4: The path of atoms during the fcc→bcc martensitic transformation in the 1.4 wt% C supercell. (a) The initial fcc structure, (b) the per-atom potential energy for each atom of the initial fcc structure, (c) $\epsilon = 2.8\%$ and (d) $\epsilon = 4\%$. The black arrows represent displacements, which are magnified 2.5 times for better observation. Atoms in (a), (c), and (d) are colored by the a-CNA method: bcc (blue), fcc (green), unidentified (grey), and carbon (pink).

the phase transformation. And this shape change of the supercell is conceptually consistent with the Bain transformation mechanism. The specific path of the atoms during this process can be observed in Fig. 4. Comparing Figs. 4(a) and 4(b) shows that the Fe atoms nearest to the C atoms have lower potential energy. Figs. 4(c) and 4(d) reveal the nucleation and growth of bcc structure, respectively. It is apparent that the nucleation position of bcc is more dispersed than that of 0.2 wt% C. The displacements of atoms are influenced by the C atom distribution. The C atoms stabilize the nearest Fe atoms and thus results in different deformability of different regions in the supercell. The C atoms and its nearest Fe atoms are like barriers for the displacement of the other Fe atoms. Therefore, strain concentration occurs during the deformation process and leads to phase transformation localization. This fcc→bcc transformation mechanism is driven by the local shear. Comparing with the 0.2 wt% C, the 1.4 wt% C supercell has no substructure that might result from the high shear barrier as the C addition. Similar heterogeneous nucleation has been found in the research of Ou [30], he found that the phase interfaces, free surfaces and defects would affect the nucleation of martensite, and concluded that the martensitic transformation

will occur preferentially in areas where strain is present. The fcc→bcc martensitic transformation in our work is the Bain model, which is not observed in most experimental results. This is because the simulation situation in this work is unique, e.g., the pressure in the supercell is controlled to be 0 MPa in Y- and Z-axis. By contrast, in the real situation, the fcc austenite matrix restricts the formation of the bcc martensite. Under similar simulation conditions, the fcc→bcc martensitic transformation has been found to follow the Bain model in the previous MD researches [25,31]. Sun et al. [31] performed a uniaxial tensile MD simulation on a Cu film and traced the distance evolutions between the adjacent Cu atoms. They found that the fcc→bcc martensitic transformation was exactly corresponding to the Bain model. In addition, Engin and Urbassek [25] found that the temperature-induced martensitic transformation in pure Fe also followed the Bain model.

Deformation mechanism of bcc

After the fcc→bcc phase transformation, the bcc martensitic product continues to deform. Figure 5 shows the snapshots of bcc deformation of the 0.2 wt% supercell, and the

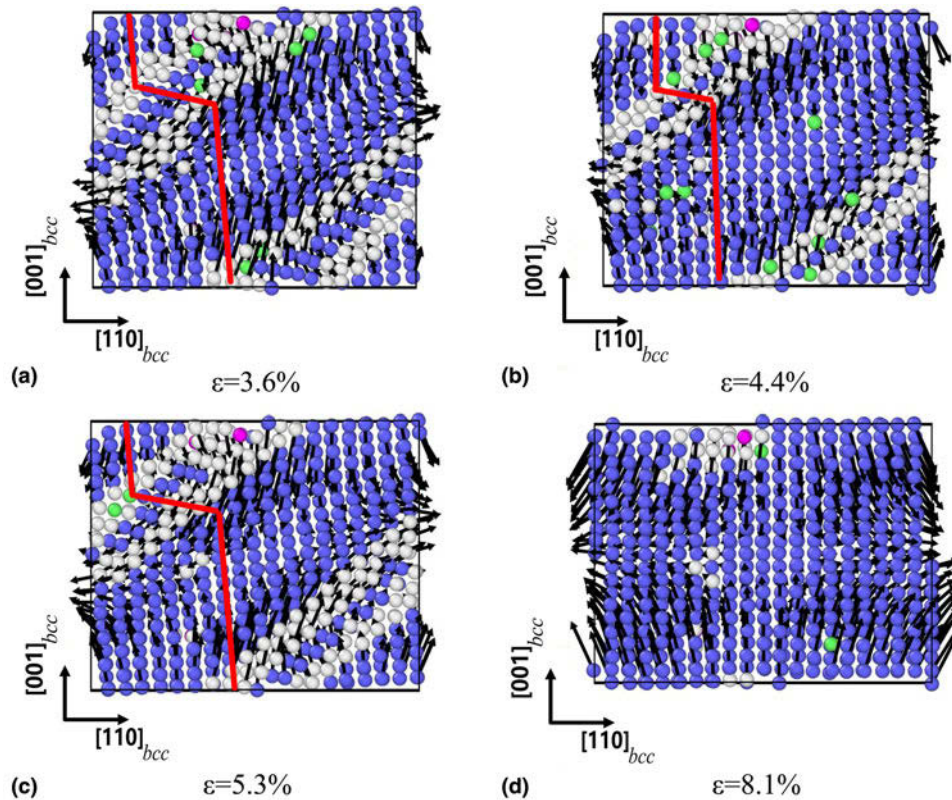


Figure 5: The deformation mechanism of bcc for 0.2 wt% C: (a) $\epsilon = 3.6\%$, (b) $\epsilon = 4.4\%$, (c) $\epsilon = 5.3\%$, and (d) $\epsilon = 8.1\%$. The black arrows represent displacements, which are magnified 2.5 times. Atoms are colored by the a-CNA method: bcc (blue), fcc (green), unidentified (grey), and carbon (pink).

corresponding stresses are illustrated by the red pentagrams in Fig. 1(c). In Fig. 5(a), the twinning bcc structure at $\epsilon = 3.6\%$ is distorted by shear, and the displacements of atoms indicate that there are significant internal stresses in the supercell. With further deformation, the boundary migration of twinning bcc structure occurs as evident from Fig. 5(b), as the width of the middle twinning is reduced as indicated by the red lines. Meanwhile, the displacements of atoms decrease as the atoms move toward their initial position. The distortion of the bcc structure recovers a little, which means that the internal stress decreases. For the whole supercell, the rapid drop of *X*-axis stress as shown in Fig. 1(c) evidences the reduction of internal pressure. As the deformation continues, the shear deformation increases again, which leads to the twinning boundary migration and *X*-axis stress increases as evident from Figs. 1(c) and 1(c). After several cycles of twinning boundary migration, the bcc twinning structure annihilates from the strain of 7.7–8.1% and accompanied by a drop in stress. At $\epsilon = 8.1\%$, the supercell completely transforms into a natural bcc structure. Subsequently, the bcc structure undergoes elastic deformation. This bcc deformation mechanism was first proposed by Ölander [32] in Au–Cd alloy and was defined as rubber-like elasticity of martensite. This reversion phenomenon of internal bcc twinning substructures is known as detwinning, and

Basinski and Christian [33] explained that the detwinning was forced by stress by using the twinning dislocation theory. In a recent study, Ping et al. [34] observed the detwinning process in the low C concentration Fe–C alloys during the quenching and concluded that the driving force was the instability of the twinning boundary region. Burkart and Read [35] observed that the twin boundaries migrate and finally disappear during the straining process and found the smaller the axial ratio (*c/a*), the more easily (101) twins nucleated and the more pronounced the rubber-like characteristics were. This rule is consistent with the results of our study. For low C concentration (small axial ratio) like 0.2 wt% C, this rubber-like elasticity characteristic is obvious as illustrated above. By contrast, the bcc structure with a high C concentration like 1.4 wt% C only undergoes a short elastic deformation before the bcc→hcp phase transformation. The rubber-like elasticity is not observed so there is no detailed display.

As the above-mentioned stress–strain curves, the elastic constant in the *X*-axis of the supercell decreases as the C addition. The elastic constant of Hooke’s law is represented in terms of tensor. The crystal structure is distorted as the C atoms are preferably distributed along the *c*-axis after the fcc→bcc phase transformation. Thus, the martensitic product crystal structure is distorted to body-centered tetragonal,

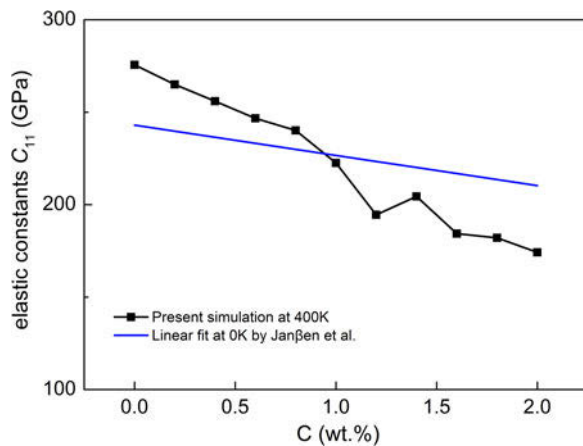


Figure 6: Elastic constant C_{11} as a function of C concentration: Gunkelmann et al. [36] data evaluated at 0 K with the potential by Lee [39]. The present simulation data evaluated at 400 K with the potential by Lee [39].

which belongs to the tetragonal system, and there are six independent elastic constants. In the present work, the elastic constant along the X-axis is C_{11} . Gunkelmann et al. [36] have investigated the elastic constants of α' (bcc or bct) Fe–C martensite single crystal by experiments and the molecular dynamics method. They found that the elastic constant C_{11} decreased with an increase in the C concentration by using the potential of Becquart et al. [37]. And on this basis, Janßen et al. [38] compared six different Fe–C potentials including Lee potential to investigate the elastic constant of Fe–C alloys. The elastic tensor of the bcc structure supercells is calculated, which are converted from the dump files at the strain of 13% of the deformation process. The script provided in LAMMPS is used, and the simulation temperature is controlled at 400 K. The elastic constant C_{11} of our investigation and the results from Janßen et al. [38] are shown in Fig. 6. It is evident that the elastic constant C_{11} of the two simulation results both shows the decreasing trend with the C addition. This effect can be explained by the volume expansion result of C addition, which weakens the bonding energy and comforts the elastic constants [36]. The reason for the increase of C_{11} at 1.4 wt% C seems to be a deviation of C_{11} at 1.2 wt% C, which is a single tension data from Fig. 1.

Phase transformation mechanism of bcc→hcp

When the elastic deformation of bcc reaches a certain strain, the bcc→hcp transformation will take place to resolve the increasing strain. As is well known, for pure Fe and Fe–C alloys, the bcc→hcp transformation process takes place under large deformation. In our present study, this transformation mechanism also occurs in the Fe–C alloys subjected to external strain. Figure 7 presents the bcc→hcp phase transformation mechanism in the 0.2 wt% C supercell. Figure 7(a) shows the atomic structure of three $(\bar{1}\bar{1}0)_{\text{bcc}}$ layers during the phase

transformation. The black rectangle in the bcc structure (blue atoms) represents the $(\bar{1}\bar{1}0)_{\text{bcc}}$ plane, while the black regular hexagon in the hcp structure (red atoms) represents the $(0001)_{\text{hcp}}$ plane. The $[11\bar{2}0]_{\text{hcp}}$ crystal direction is parallel to the $[111]_{\text{bcc}}$ direction, which indicates that the invariant direction is $[111]_{\text{bcc}}$ and the lattice orientation relationships are

$$(\bar{1}\bar{1}0)_{\text{bcc}}(0001)_{\text{hcp}} \text{ and } [111]_{\text{bcc}}[11\bar{2}0]_{\text{hcp}}$$

These orientation relationships are the same as the Burgers relationship. Burgers [9] first proposed this bcc→hcp transformation mechanism when studied the transformation in Zr by X-ray diffraction. On the other hand, these three layers in Fig. 7(a) can be regarded as close-packed layers of $(110)_{\text{bcc}}$ plane, and the crystal structures before and after phase transformation of these close-packed layers are shown in Figs. 7 (b) and 7(c). The displacements of the atoms indicate that the adjacent bcc close-packed layers move in opposite directions, $\pm[110]_{\text{bcc}}$, which results in the bcc-phase transforms to the hcp phase. For the entire supercell shown in Figs. 7(d) and 7(e), alternate shear displacement takes place on every other bcc close-packed layer, the hcp structure is generated. When the two adjacent layers move in the same direction, the resulting structure is the twin boundary of the hcp structure, which is identified as fcc layers as shown in Fig. 7(e).

The transformation from bcc phase to hcp phase in the 1.4 wt% C supercell is illustrated in Fig. 8. The transformation process of this supercell is much slower than the supercell containing 0.2 wt% C. According to the atomic structure change during the transformation process shown in Figs. 8(a)–8(c), the phase transformation occurs in a small area and has a sequence, which is significantly different from the simultaneous phase transformation of all bcc close-packed layers in the 0.2 wt% C supercell. This phenomenon can be attributed to the interstitial solution of C atoms. The C atoms distort the crystal lattice and decrease the potential energy of its nearest and second-nearest Fe atoms, as shown in Fig. 8(d), which leads to the inhomogeneity of the mechanical properties in the simulation supercell. Moreover, this inhomogeneity results in different deformation mechanisms of atoms in the supercell, as illustrated in Fig. 8(e). In this figure, the bcc→hcp phase transformation caused by the shearing motion of the close-packed layers and the elastic deformation of the bcc atoms occurs simultaneously. It seems that this bcc→hcp phase transformation has a priority order and occurs preferentially in areas surrounded by C atoms.

Dislocation analysis during the phase transformation

The martensite transformation of Fe–C steels is actually assisted by dislocations. In the present simulation, the

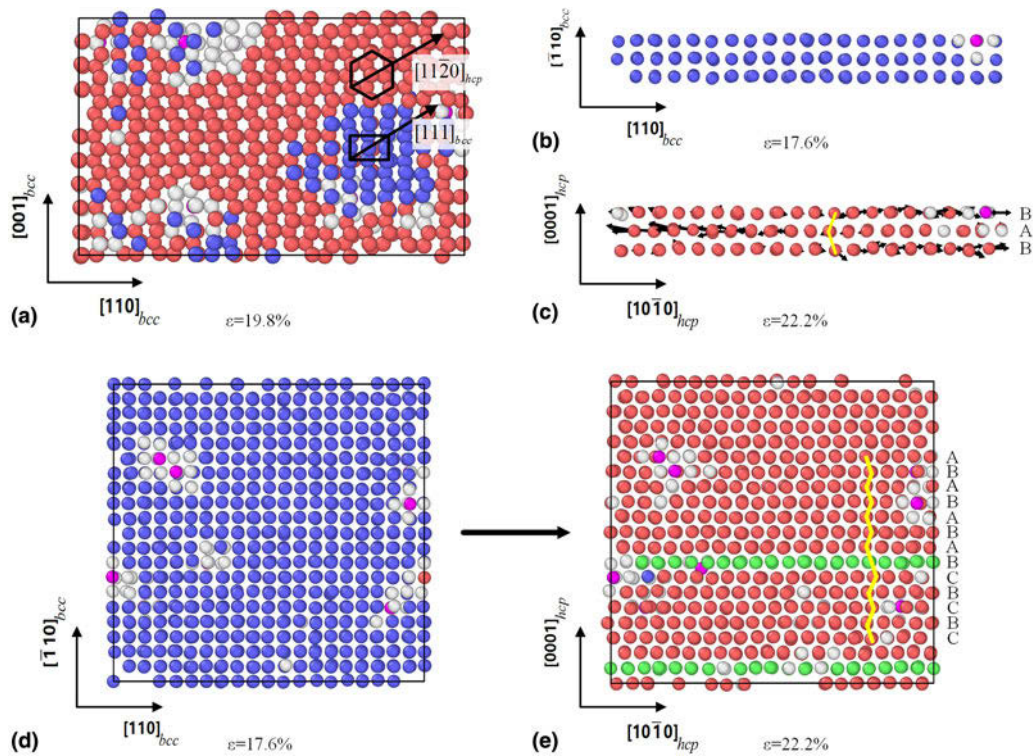


Figure 7: The bcc→hcp phase transformation mechanism in the 0.2 wt% C supercell. (a) Three layers of atoms perpendicular to $[\bar{1}10]_{bcc}$ (Y-axis) in the supercell during the phase transformation. (b) The bcc structure of these atoms before the transformation from the top view of (a). The hcp structure of these atoms after the transformation is shown in (c). (d) and (e) show the atomic structure of supercell before and after the phase transformation, respectively. The black arrows represent displacements, which are magnified three times for better observation. Atoms are colored by the a-CNA method: bcc (blue), fcc (green), hcp (red), unidentified (grey), and carbon (pink).

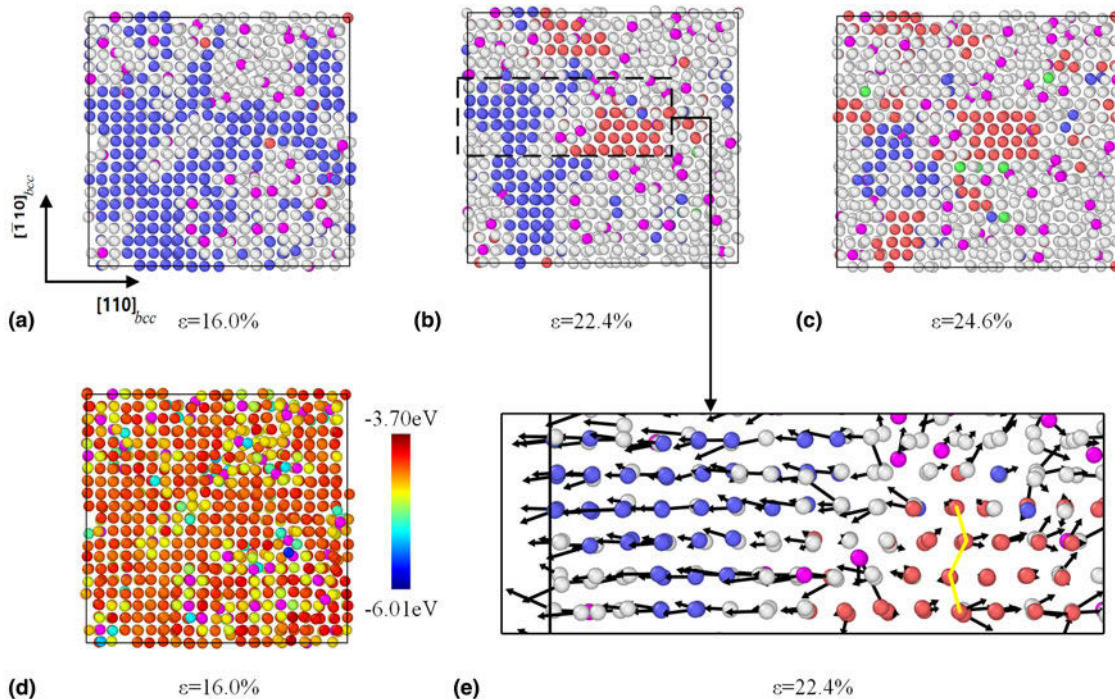


Figure 8: The bcc→hcp phase transformation mechanism in the 1.4 wt% C supercell. (a–c) Close-packed layers perpendicular to $[\bar{1}10]_{bcc}$ (Y-axis) of the supercell at $\epsilon = 16.0, 22.4,$ and 24.6% , respectively. (d) The per-atom potential energy for each atom in (a). (e) is a representative area of (b) and shows the atomic displacements relative to the positions of the atoms in (a). The black arrows represent displacements, which are magnified three times for better observation. Atoms in (a)–(c) and (e) are colored by the a-CNA method: bcc (blue), fcc (green), red (hcp), unidentified (grey), and carbon (pink).

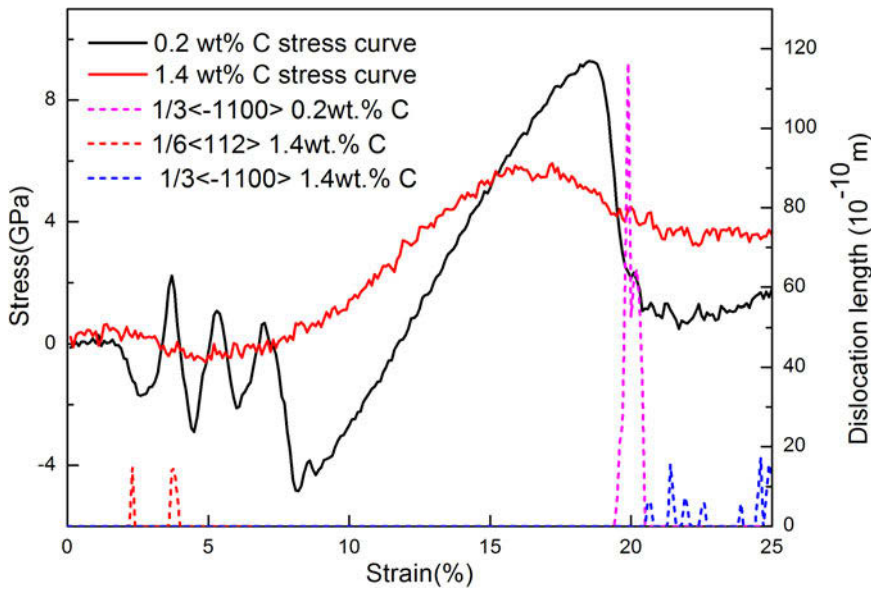


Figure 9: The comparison of dislocation analysis (DXA) [40] and corresponding strain–stress curves for 0.2% C and 1.4% C supercells during deformation simulation.

phenomenons of dislocations appear in high C and low C supercells are quite different. Figure 9 shows the dislocation analysis for 0.2 and 1.4 wt% C supercells during the deformation. For 0.2 wt% C supercell, no dislocation appears during the fcc→bcc phase transformation. The transformation is achieved by the atoms move along the specific slip planes which are caused by the shear stress. By comparison, some $1/6\langle 112 \rangle$ Shockley partial dislocations are generated and soon

annihilated in the 1.4 wt% C supercell during this process. The dislocations are represented by green lines shown in Fig. 10(a). This is because too many C atoms impede the shear movement of Fe atoms along the atomic plane, which causes the stacking fault to form on the part of the atomic plane. It is well known that the Shockley partial dislocations are formed in the junction of the stacking fault and the perfect crystal. During the bcc→hcp phase transformation, the $1/$

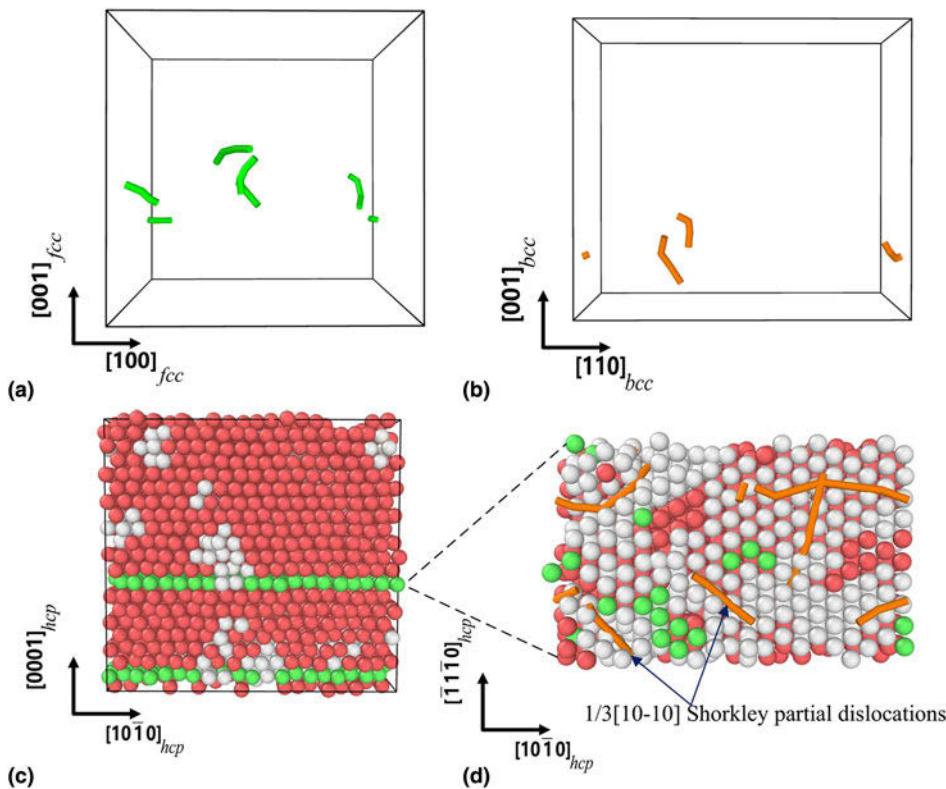


Figure 10: The snapshots of dislocation during the phase transformation: (a) the green lines are $1/6\langle 112 \rangle$ Shockley partial dislocations in the 1.4 wt% C supercell at $\epsilon = 2.6\%$. (b) The orange lines are $1/3\langle -1100 \rangle$ Shockley partial dislocations in the 1.4 wt% C supercell at $\epsilon = 22\%$. (c) Twin structure in the hcp phase of 0.2 wt% C supercell at $\epsilon = 20\%$. (d) The planform of the layer where twin boundary generates, the orange lines are $1/3\langle -1100 \rangle$ Shockley partial dislocation, and they only occur in the twin boundary layer in (c).

$3\langle 1100 \rangle$ Shockley partial dislocations take place in both the 0.2 and 1.4 wt% C supercells but in different ways. In 0.2 wt% C supercell, the bcc→hcp phase transformation is almost instantaneous, and the $1/3\langle 1100 \rangle$ Shockley partial dislocations burst only in this very short process. The dislocations take place where the twin boundaries of the hcp phase exactly generate, as shown in Figs. 10(c) and 10(d). In contrast, the Shockley partial dislocations take place locally and continuously in the 1.4 wt% C supercell as shown in Fig. 10(b). This is because the bcc→hcp phase transformation is a continuous and sequential process as discussed in Sec. 3.4.

CONCLUSION

It has been shown by MD simulations that interstitial C atoms affect the deformation mechanism of the parent fcc Fe–C alloys. The Lee MEAM potential used demonstrates its reliable predictability in phase transformation and reproduces the properties of various phases in each stage of deformation. The fcc structure under uniaxial tensile first undergoes the fcc→bcc martensitic transformation, then the deformation of bcc martensite, and finally the bcc→hcp martensitic transformation. However, in initial structures with various C concentrations, these deformation processes and corresponding stress–strain curves are quite different. The effect of C concentration on the deformation mechanisms of the Fe–C system is as follows:

- (i) *The fcc→bcc martensitic transformation:* For lower C concentration, the phase transformation mechanism is a two-stage shear mechanism. The first shear stage makes the most fcc atoms transform to bcc atoms, the second shear stage forces the rest transformation take place, which is accompanied with the formation of the bcc martensitic twinning substructure. With the C concentration increasing, the C atoms impede the shear movements of Fe atoms, which result in the large-scale phase transformation difficult to start. Thus, the localized phase transformation mechanism occurs in the supercell with higher C addition. The orientation relations of this transformation mechanism follow the Bain model.
- (ii) *The deformation of bcc martensite:* The low C bcc martensitic product has the twinning substructures and exhibits rubber-like elasticity property. With the strain increasing, the migration of the bcc twinning boundary occurs repeatedly; finally, the bcc twinning substructures transform to natural bcc structures (detwinning). After that, the bcc structure undergoes elastic deformation. While the high C bcc martensite has no substructure and only experiences elastic deformation. The elastic constant of the bcc martensite decreases with C addition in all simulated concentration ranges.
- (iii) *The bcc→hcp martensitic transformation:* This mechanism of all simulated cases accords the Burgers path. Almost all bcc atoms transform to hcp atoms at the same time in the supercell with low C concentration. The C atoms addition leads to the inhomogeneity of the mechanical properties in the bcc structure, resulting in the simultaneous bcc→hcp phase transformation and the elastic deformation of the bcc phase in the supercell with high C concentration.
- (iv) *The dislocation analysis during the transformation:* During the fcc→bcc martensitic transformation process, the dislocation $1/6\langle 112 \rangle$ Shockley partial dislocations take place in the high C supercells, and no dislocation observed in the pure and low C supercells. For the bcc→hcp martensitic transformation, the $1/3\langle 1100 \rangle$ Shockley partial dislocations occur instantaneously in low C supercells but continuously in high C supercells.

SIMULATION METHODOLOGY

In the present work, the Fe–C-modified embedded-atom method (MEAM) interatomic potential developed by Lee was used, which can reflect the effect of interstitial C atoms on the deformation mechanism and phase transformation of various crystal structures for Fe–C alloys [39]. Compared with the original first nearest-neighbor MEAM (1NN MEAM) potential, Lee MEAM potential considers the second nearest-neighbor interactions, so it is known as the second-neighbor MEAM (2NN MEAM). The original intention of developing 2NN MEAM potential is to solve the problems of the 1NN MEAM potential and provide a useful tool for studying the solid-state phase transformation [41,42]. Lee MEAM potential can reproduce the properties of Fe and C atoms within the entire composition range, the concentration of C from 0 to 100 wt%. Another unique advantage of this potential is that it can describe various crystal structures like bcc, fcc, and hcp by just using the same parameters or formalism [41, 42]. Moreover, Mohammadzadeh and Mohammadzadeh [43] calculated the stacking fault energy (SFE) of fcc crystal structures of Fe–C alloys by using Lee MEAM potential, and the resulting SFE values were in good agreement with the trend of the first-principle calculations [44]. In recent studies [45,46], SFE has been proved to be closely related to the deformation mechanism in austenitic alloys, including the martensitic transformation. The free-energy difference of bcc and fcc phases of pure Fe and Fe–C alloys was also calculated using the Frenkel–Ladd method [47] (a thermodynamic integration method) by Lee MEAM potential. The results indicate that in all cases of this study, the bcc phase is stable and the fcc phase is metastable at 400 K, while the free-energy difference is too small to trigger the fcc phase spontaneously transforms to the bcc

phase. The initial fcc phase of different sizes and different C concentrations maintains stable after equilibrium relaxation at 400 K of 800 ps, which is much longer than the entire simulation time. This result can confirm the martensitic transformation is forced by the mechanical loading, not by the strain or stress caused by the thermal fluctuations. Based on the above arguments, using Lee MEAM potential to investigate the martensitic transformation process in this work is entirely feasible.

LAMMPS open source code [48] is employed for the molecular dynamics study. The supercells are a single crystal of fcc austenite, and their sizes are $10 \times 10 \times 10$, $20 \times 20 \times 20$, and $30 \times 30 \times 30$ unit cells in X , Y , and Z directions, respectively. The length of the fcc lattice constant is 3.64 Å. The number of iron atoms in supercells of different sizes is 4000, 32,000, and 108,000, respectively. The X -axis is along the [100] orientation of the initial fcc crystal structure, the Y -axis is along the [010] orientation, and the Z -axis is along the [001] orientation. Interstitial C atoms are randomly added to the octahedral sites of the fcc crystal structure since it is well known that the octahedral sites are the most stable sites for C atom, and this distribution method has been successfully employed in previous studies [22,23]. The concentrations of C used are 0, 0.2, 0.4, 0.6, 0.8, 1.0, 1.2, 1.4, 1.6, 1.8, and 2.0 wt%, from pure Fe to the saturation concentration of C in austenite. Three randomly distributed supercells for each C concentration are simulated. The periodic boundary conditions are applied in all three directions. The energy of the simulation system is minimized at 0 K by the conjugate gradient algorithm. As mentioned above, the initial fcc phase of all C concentrations are metastable at 400 K. Therefore, the relaxation temperature and deformation temperature are set at 400 K for better analysis of the phase transformation caused by deformation. The constant pressure and temperature ensemble (NPT ensemble) is employed to relax the system at 400 K for 200 ps by using a Nosé–Hoover thermostat. After equilibration, the simulation cell is deformed in the X -axis direction at a strain rate of 1×10^{10} /s. Meanwhile, the pressures of Y - and Z -axis direction boundaries are controlled to 0 MPa, and the values of stress and strain in the X -axis direction of the supercell are recorded. The OVITO software [14] is used to visualize the simulation process, the a-CNA [49] is performed to classify the structural type of atoms, and the DXA [40] is used to identify the dislocations in crystal.

Supplementary material

To view supplementary material for this article, please visit <https://doi.org/10.1557/jmr.2020.154>.

References

1. **P.M. Kelly:** *Phase Transformations in Steels* (Woodhead Publishing, Cambridge, UK, 2012).
2. **Z. Nishiyama:** *5-Conditions for Martensite Formation and Stabilization of Austenite in Martensitic Transformation* (Academic Press, London, UK, 1978).
3. **A. Sauveur:** What is a steel another answer. *Iron Age* **113**, 581 (1924).
4. **C.X. Huang, G. Yang, Y.L. Gao, S.D. Wu, and S.X. Li:** Investigation on the nucleation mechanism of deformation-induced martensite in an austenitic stainless steel under severe plastic deformation. *J. Mater. Res.* **22**, 724 (2011).
5. **U. Kühn, J. Romberg, N. Mattern, H. Wendrock, and J. Eckert:** Transformation-induced plasticity in Fe–Cr–V–C. *J. Mater. Res.* **25**, 368 (2011).
6. **E.C. Bain:** The nature of martensite. *Trans. AIME* **79**, 25 (1924).
7. **G. Kurdjumov and G. Sachs:** Über den Mechanismus der Stahlhartung. *Zeitschr. Phys.* **74**, 325 (1930).
8. **Z. Nishiyama:** X-ray investigation of the mechanism of the transformation from face centered cubic lattice to body centered cubic. *Sci. Rep. Tohoku Univ.* **23**, 637 (1934).
9. **W.G. Burgers:** On the process of transition of the cubic-body-centered modification into the hexagonal-close-packed modification of zirconium. *Physica* **1**, 561 (1934).
10. **A.J. Bogers and W.G. Burgers:** Partial dislocations on the {110} planes in the B.C.C. lattice and the transition of the F.C.C. into the B.C.C. lattice. *Acta Metall.* **12**, 255 (1964).
11. **G.B. Olson and M. Cohen:** A mechanism for the strain-induced nucleation of martensitic transformations. *J. Less-Common Met.* **28**, 107 (1972).
12. **Z. Nishiyama:** *6-The Crystallographic Theory of Martensitic Transformations in Martensitic Transformation* (Academic Press, London, UK, 1978).
13. **R. Bunshah and R. Mehl:** Rate of propagation of martensite. *Trans. AIME* **197**, 1251 (1953).
14. **A. Stukowski:** Visualization and analysis of atomistic simulation data with OVITO: The Open Visualization Tool. *Modell. Simul. Mater. Sci. Eng.* **18**, 2154 (2010).
15. **J. Li:** AtomEye: An efficient atomistic configuration viewer. *Model. Simul. Mater. Sci.* **11**, 173 (2003).
16. **C. Bos, J. Sietsma, and B.J. Thijssse:** Molecular dynamics simulation of interface dynamics during the fcc-bcc transformation of a martensitic nature. *Phys. Rev. B* **73**, 104 (2006).
17. **B. Wang, E. Sak-Saracino, N. Gunkelmann, and H.M. Urbassek:** Molecular-dynamics study of the $\alpha \leftrightarrow \gamma$ phase transition in Fe–C. *Comput. Mater. Sci.* **82**, 399 (2014).
18. **P. Entel, R. Meyer, K. Kadau, H.C. Herper, and E. Hoffmann:** Martensitic transformations: First-principles calculations combined with molecular-dynamics simulations. *Eur. Phys. J. B* **5**, 379 (1998).
19. **S. Karewar, J. Sietsma, and M.J. Santofimia:** Effect of pre-existing defects in the parent fcc phase on atomistic mechanisms during

- the martensitic transformation in pure Fe: A molecular dynamics study. *Acta Mater.* **142**, 71 (2018).
20. **Z. Nishiyama:** *3-Crystallography of Martensites—Special Phenomena in Martensitic Transformation* (Academic Press, London, UK, 1978).
 21. **T.Q. Nguyen, K. Sato, and Y. Shibutani:** Development of Fe-C interatomic potential for carbon impurities in α -iron. *Comput. Mater. Sci.* **150**, 510 (2018).
 22. **B. Wang, E. Sak-Saracino, L. Sandoval, and H.M. Urbassek:** Martensitic and austenitic phase transformations in Fe-C nanowires. *Modell. Simul. Mater. Sci. Eng.* **22**, 045003 (2014).
 23. **S. Karewar, J. Sietsma, and M. Santofimia:** Effect of C on the martensitic transformation in Fe-C alloys in the presence of pre-existing defects: A molecular dynamics study. *Crystals* **9**, 99 (2019).
 24. **H.-T. Luu and N. Gunkelmann:** Pressure-induced phase transformations in Fe-C: Molecular dynamics approach. *Comput. Mater. Sci.* **162**, 295 (2019).
 25. **C. Engin and H.M. Urbassek:** Molecular-dynamics investigation of the fcc \rightarrow bcc phase transformation in Fe. *Comput. Mater. Sci.* **41**, 297 (2008).
 26. **R.L. Patterson and G. Wayman:** The crystallography and growth of partially-twinned martensite plates in Fe-Ni alloys. *Acta Metall.* **14**, 347 (1966).
 27. **K.-i. Shimizu:** Direct observation of sub-structures of the martensite in Fe-Ni alloy by means of electron microscopy. *J. Phys. Soc. Jpn.* **17**, 508 (1962).
 28. **R. Patterson and C. Wayman:** Internal twinning in ferrous martensites. *Acta Metall.* **12**, 1306 (1964).
 29. **A.B. Greninger and A.R. Troiano:** The mechanism of Martensite formation. *JOM* **1**, 590 (1949).
 30. **X. Ou:** Molecular dynamics simulations of fcc-to-bcc transformation in pure iron: A review. *Mater. Sci. Technol.* **33**, 822 (2016).
 31. **B. Sun, W.Z. Ouyang, J.J. Ren, L.W. Mi, and W. Guo:** Fcc \rightarrow bcc \rightarrow hcp successive phase transformations in the strained ultrathin copper film: A molecular dynamic simulation study. *Mater. Chem. Phys.* **223**, 171 (2019).
 32. **A. Ölander:** The crystal structure of AuCd. *Z. Kristallogr. Crystall. Mater.* **83**, 145 (1932).
 33. **Z.S. Basinski and J.W. Christian:** Crystallography of deformation by twin boundary movements in indium-thallium alloys. *Acta Metall.* **2**, 101 (1954).
 34. **D.H. Ping, S.Q. Guo, M. Imura, X. Liu, T. Ohmura, M. Ohnuma, X. Lu, T. Abe, and H. Onodera:** Lath formation mechanisms and twinning as lath martensite substructures in an ultra low-carbon iron alloy. *Sci. Rep.* **8**, 14264 (2018).
 35. **M. Burkart and T. Read:** Diffusionless phase change in the Indium-Thallium system. *Trans. AIMME* **197**, 1516 (1953).
 36. **N. Gunkelmann, H. Ledbetter, and H.M. Urbassek:** Experimental and atomistic study of the elastic properties of α' Fe-C martensite. *Acta Mater.* **60**, 4901 (2012).
 37. **C.S. Becquart, J.M. Raulot, G. Bencteux, C. Domain, M. Perez, S. Garruchet, and H. Nguyen:** Atomistic modeling of an Fe system with a small concentration of C. *Comput. Mater. Sci.* **40**, 119 (2007).
 38. **J. Janßen, N. Gunkelmann, and H.M. Urbassek:** Influence of C concentration on elastic moduli of α' -Fe $_{1-x}$ C $_x$ alloys. *Philos. Mag.* **96**, 1448 (2016).
 39. **B.-J. Lee:** A modified embedded-atom method interatomic potential for the Fe-C system. *Acta Mater.* **54**, 701 (2006).
 40. **A. Stukowski, V.V. Bulatov, and A. Arsenlis:** Automated identification and indexing of dislocations in crystal interfaces. *Modell. Simul. Mater. Sci.* **20**, 085007 (2012).
 41. **B.-J. Lee and M. Baskes:** Second nearest-neighbor modified embedded-atom-method potential. *Phys. Rev. B* **62**, 8564 (2000).
 42. **B.-J. Lee, M.I. Baskes, H. Kim, and Y. Koo Cho:** Second nearest-neighbor modified embedded atom method potential for BCC transition metals. *Phys. Rev. B* **64**, 184102 (2001).
 43. **M. Mohammadzadeh and R. Mohammadzadeh:** Effect of interstitial and substitution alloying elements on the intrinsic stacking fault energy of nanocrystalline fcc-iron by atomistic simulation study. *Appl. Phys. A* **123**, 720 (2017).
 44. **S. Lu, R. Li, K. Kadas, H. Zhang, Y. Tian, S.K. Kwon, K. Kokko, Q.M. Hu, S. Hertzman, and L. Vitos:** Stacking fault energy of C-alloyed steels: The effect of magnetism. *Acta Mater.* **122**, 72 (2017).
 45. **T.-H. Lee, E. Shin, C.-S. Oh, H.-Y. Ha, and S.-J. Kim:** Correlation between stacking fault energy and deformation microstructure in high-interstitial-alloyed austenitic steels. *Acta Mater.* **58**, 3173 (2010).
 46. **T. Huang, W. Dan, and W. Zhang:** Study on the strain hardening behaviors of TWIP/TRIP steels. *Metall. Mater. Trans. A* **48**, 4553 (2017).
 47. **R. Freitas, M. Asta, and M. de Koning:** Nonequilibrium free-energy calculation of solids using LAMMPS. *Comput. Mater. Sci.* **112**, 333 (2016).
 48. **S. Plimpton:** Fast parallel algorithms for short-range molecular dynamics. *J. Comput. Phys.* **117**, 1 (1995).
 49. **A. Stukowski:** Structure identification methods for atomistic simulations of crystalline materials. *Modell. Simul. Mater. Sci. Eng.* **20**, 45021 (2012).